9.7   AN EVOLUTIONARY APPROACH TO NONHYDROSTATIC MODELING

Zavisa Janjic*, Tom Black, Matthew Pyle, Hui-ya Chuang, Eric Rogers and Geoff DiMego
National Centers for Environmental Prediction, Camp Springs, Maryland

1. INTRODUCTION

With constantly increasing horizontal resolution, numerical weather prediction models are approaching limits of validity of the hydrostatic approximation. Although considerable experience with nonhydrostatic models has been accumulated on the scales of convective clouds and storms, numerical weather prediction (NWP) deals with motions on a much wider range of temporal and spatial scales. Difficulties that may not be significant, or may go unnoticed on the small scales, may become important in NWP applications. For example, an erratic gain or loss of mass would be hard to tolerate in an operational environment. Problems may also arise with spurious motions generated in the upper levels by the nonhydrostatic dynamics and numerics. Forcing the variables in the top model layers toward a steady state in response to this problem is inadequate for NWP, and, on the other hand, specifying time dependent computational top boundary conditions would limit the ability of the nested model to produce more accurate forecasts than the parent model.

Having in mind these considerations, a novel approach (Janjic et al., 2001; Janjic, 2003) has been applied in the NCEP Nonhydrostatic Meso Model (NMM) that has been developed within the Weather Research and Forecasting (WRF) initiative. Namely, instead of extending cloud models to larger spatial and temporal scales, the hydrostatic approximation is relaxed in a hydrostatic model formulation based on modeling principles proven in NWP practice. These principles have been set up by Janjic (1977, 1979, 1984) and have been applied and thoroughly tested in NWP and regional climate applications of the NCEP Eta model.

_____
*Corresponding author address: Zavisa I. Janjic,
National Centers for Environmental Prediction,
5200 Auth Rd., Camp Springs, MD 20746;
e-mail: Zavisa.Janjic@noaa.gov

By relaxing the hydrostatic approximation the applicability of the hydrostatic formulation is extended to nonhydrostatic motions, and at the same time the favorable features of the hydrostatic formulation are preserved. In other words, following an evolutionary approach, the nonhydrostatic NWP model is built on NWP experience.

With this approach the nonhydrostatic equations are split into two parts: (a) the part that corresponds to the hydrostatic system, except for corrections due to the vertical acceleration, and (b) the part that allows computation of the corrections appearing in the first system. The described procedure does not require any linearization or additional approximation. Note that the separation of the nonhydrostatic terms shows in a transparent way where, how and how much the hydrostatic approximation affects the equations. Moreover, the nonhydrostatic effects are introduced in the form of an add–on nonhydrostatic module that can be turned on or off depending on model resolution. In this way the nonhydrostatic model can be run in the hydrostatic mode at lower resolutions with no extra cost.

2. MODEL EQUATIONS

For simplicity, as a representative of mass based vertical coordinates, consider the sigma coordinate (Phillips, 1957)

$$\sigma = \frac{(\pi - \pi_t)}{\mu}, \qquad (2.1)$$

where π is the hydrostatic pressure, and μ represents the difference in hydrostatic pressure between the base and the top of the model column

$$\mu = \pi_s - \pi_t . \qquad (2.2)$$

Here, π_s and π_t stand for the hydrostatic pressures at the surface and at the top of the model atmosphere. Then, the equations governing a dry, inviscid and adiabatic nonhydrostatic atmosphere are (Janjic et al., 2001; Janjic 2003)

$$\frac{d\mathbf{v}}{dt} = -(1+\varepsilon)\nabla_\sigma \Phi - \alpha \nabla_\sigma p + f\mathbf{k} \times \mathbf{v}, \quad (2.3)$$

$$\begin{aligned}\frac{\partial T}{\partial t} = &-\mathbf{v} \bullet \nabla_\sigma T - \dot{\sigma}\frac{\partial T}{\partial \sigma} \\ &+ \frac{\alpha}{c_p}(\frac{\partial p}{\partial t} + \mathbf{v} \bullet \nabla_\sigma p + \dot{\sigma}\frac{\partial p}{\partial \sigma})\end{aligned}, \quad (2.4)$$

$$\sigma \frac{\partial \mu}{\partial t} = -\int_0^\sigma [\nabla_\sigma \cdot (\mu\mathbf{v}) + \frac{\partial(\mu\dot{\sigma})}{\partial \sigma}]d\sigma', \quad (2.5)$$

$$p\alpha = RT, \quad (2.6)$$

$$\frac{1}{\mu}\frac{\partial \Phi}{\partial \sigma} = -\alpha, \quad (2.7)$$

$$w = \frac{1}{g}(\frac{\partial \Phi}{\partial t} + \mathbf{v} \bullet \nabla_\sigma \Phi + \dot{\sigma}\frac{\partial \Phi}{\partial \sigma}), \quad (2.8)$$

$$\varepsilon \equiv \frac{1}{g}\frac{dw}{dt}, \quad (2.9)$$

$$\frac{\partial p}{\partial \pi} = 1 + \varepsilon. \quad (2.10)$$

Here, in the order of appearance, $\mathbf{v}$ is the horizontal wind vector, p is the actual, nonhydrostatic pressure, R is the gas constant for dry air, T is temperature and Φ is geopotential. The other symbols used have either their usual meaning, or their meaning is self-evident. Note that Φ, w, and ε are not independent variables.

The parameter ε is the central point of the extended, nonhydrostatic dynamics. As can be readily verified, if ε is zero, the equations (2.3)-(2.7) reduce to the familiar, hydrostatic system of equations. On the synoptic scales ε is small and approaches computer round–off error. However, in case of vigorous convective storms, or strong vertical accelerations, ε can reach 10^{-3}. For this value of ε the nonhydrostatic deviation of pressure can reach 100 Pa. Bearing in mind that the typical synoptic scale horizontal pressure gradient is of the order of 100 Pa over 100 km, this suggests that significant local nonhydrostatic pressure gradients and associated circulations may develop on small scales. Nevertheless, ε remains much smaller than 1 in atmospheric flows, and therefore, the nonhydrostatic effects are of a higher order magnitude. An important consequence of this situation for discretization is that high accuracy of computation of ε does not appear to be of paramount importance, considering that the computational errors are of an even higher order than ε itself.

The method of solving of the considered system of nonhydrostatic equations is presented in more detail in Janjic et al. (2001). Further details and updates are presented in Janjic (2003). Here, only the basic principles of the discretization will be reviewed together with some additional updates, and the reader is referred to the quoted papers for details.

3. CLASSICAL NONHYDROSTATIC SOLUTIONS

In order to test the validity of the approach in the limit of highly nonhydrostatic flows, a two-dimensional model in the vertical plane was developed and run in a series of classical nonhydrostatic tests (Janjic et al., 2001). As usual for these scales, the Coriolis force was neglected. As examples, some of the results obtained in the cold and warm bubble tests (Janjic et al. 2001) will be reproduced here. For more details about these and other tests the reader is referred to Janjic et al. (2001).

Following Straka et al. (1993), in a neutrally stratified atmosphere with the potential temperature of 300^0K, an initial cold disturbance of the form

$$T(x,z) = \overline{T}(x,z)$$
$$-15\cos^2[\frac{\pi}{2}\sqrt{(\frac{x-x_c}{x_t})^2 + (\frac{z-z_c}{z_t})^2}],$$
$$if \quad \sqrt{(\frac{x-x_c}{x_t})^2 + (\frac{z-z_c}{z_t})^2} \leq 1$$

was introduced, where

$$x_c = 0 \ m, \ z_c = 3000 \, m,$$
$$x_t = 4000 \ m, \ z_t = 2000 \, m.$$

The integration domain extended 40 km in the x direction, and the free surface was located at 442 hPa, or about 6400 m. The center of the initial disturbance was in the middle of the domain in the x direction, 20 km away from either of the lateral boundaries. As in the main test in the Straka et al. (1993) study, the horizontal resolution was 100 m, and the vertical resolution was 100 m on the average. The time step was 0.3 s.

The potential temperatures after 300 s, 600 s and 900 s are displayed in Fig. 1. The area shown in the figure extends from the center of the domain to 19200 m to the right, and from the surface to 4600 m. The contour interval is $1^0 \ K$. Comparison of the results obtained in this test (Janjic et al., 2001) with the Straka et al. (1993) converged reference solution reveals very good agreement.
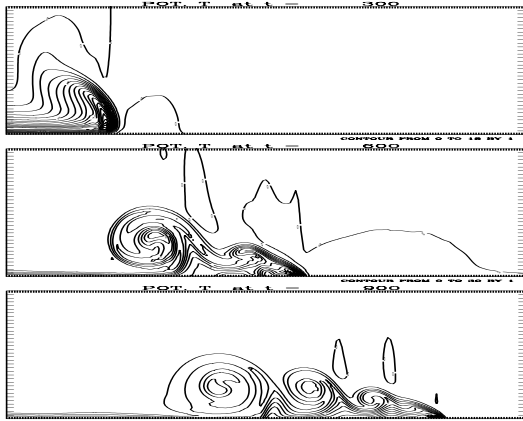

Fig. 1. The cold bubble test. Potential temperatures after 300 s, 600 s and 900 s in the right hand part of the integration domain extending from the center to 19200 m, and from the surface to 4600 m. The grid size is $\Delta z \approx \Delta x = 100$ m and $\Delta t = 0.3 \, s$. The contour interval is $1^0 \ K$.

It should be noted that hydrostatic dynamics was unable to reproduce the results shown in Fig. 1 (Janjic et al., 2001). The hydrostatic solution was computationally unstable unless the lateral diffusion was

increased by an order of magnitude. In that case, however, only very crude, qualitative resemblance to the nonhydrostatic solution was preserved.

The warm bubble test was designed following Gallus and Rancic (1996). In a neutral atmosphere with the potential temperature of $300^0 K$, an initial disturbance of the potential temperature

$$\theta(x,z) = \bar{\theta}(x,z)$$
$$+ 6.6\cos^2\left[\frac{\pi}{2}\sqrt{(\frac{x-x_c}{x_t})^2 + (\frac{z-z_c}{z_t})^2}\right],$$
$$if \quad \sqrt{(\frac{x-x_c}{x_t})^2 + (\frac{z-z_c}{z_t})^2} \le 1$$

was introduced, where

$$x_c = 0 \ m, \ z_c = 2750 \, m,$$
$$x_t = 2500 \ m, \ z_t = 2500 \, m.$$

The integration domain extended 20 km in the x direction. The free surface was located at 135 hPa, or at about 13500 m. The center of the initial disturbance was in the middle of the domain in the x direction, i.e., 10 km away from either of the lateral boundaries. The horizontal resolution was 100 m, and the vertical resolution was 100 m on the average. The time step with this spatial resolution was 0.3 s as before.

The potential temperature deviations after 360 s, 540 s, 720 s and 900 s are presented in Fig. 2. The area shown extends 16 km along the x axis, and from 1000 m to 13200 m along the z axis. The contour interval is $1^0 K$. The rate of ascent and the intensity of the disturbance agree with those reported elsewhere.

4. HORIZONTAL GRID AND HORIZONTAL COORDINATES

The choice of the horizontal grid is one of the first decisions that need to be made in the process of designing a numerical model of the atmosphere. Winninghoff (1968) and Arakawa and Lamb (1977) examined the frequencies of gravity-inertia waves obtained using second-order centered differences on
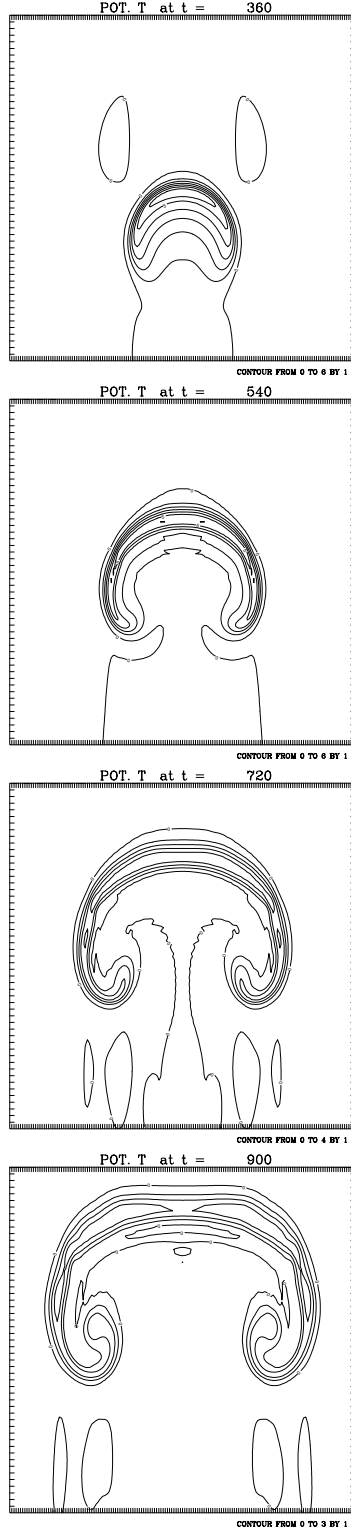
POT. T at t =   360

CONTOUR FROM 0 TO 6 BY 1

POT. T at t =   540

CONTOUR FROM 0 TO 6 BY 1

POT. T at t =   720

CONTOUR FROM 0 TO 4 BY 1

POT. T at t =   900

CONTOUR FROM 0 TO 3 BY 1

Fig. 2. The potential temperature deviation after 360 *s*, 540 *s*, 720 *s* and 900 *s* (from top to bottom) in the warm bubble test. The area shown extends 16 *km* along the *x* axis, and from 0 *m* to 13200 *m* along the *z* axis. The contour interval is 1 ^0K.

various types of rectangular horizontal grids. Compared to other grids considered, in these studies generally better agreements with the exact frequencies were obtained on the staggered grid C and on the semi-staggered grid B (or E) shown in Fig. 3. The symbol *h*
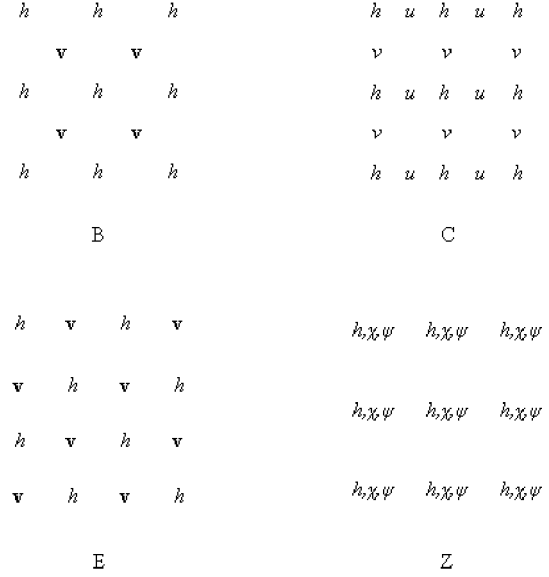
Fig. 3. The staggered grid C and the semi-staggered grids B, E and Z.

in the figure denotes the mass point variables, while the horizontal velocity vector and the velocity components are denoted, respectively, by **v**, *u* and *v*.

However, the staggered grid and the semi-staggered grids are not without problems, either. The problems on the staggered grid arise due to the averaging of the velocity components in the Coriolis force terms. On the other hand, in order to illustrate the problems on the semi-staggered grids, consider the linearized shallow water equations

$$\frac{\partial u}{\partial t} = -g\frac{\partial h}{\partial x} + fv, \quad \frac{\partial v}{\partial t} = -g\frac{\partial h}{\partial y} - fu,$$

$$\frac{\partial h}{\partial t} = -H(\frac{\partial u}{\partial x} + \frac{\partial v}{\partial y}). \qquad (4.1)$$

Here, *u* and *v* are the velocity components, *h* is the height of the free surface, *g* is gravity, *f* is the Coriolis parameter assumed to be constant, and *H* is the mean depth of the fluid.

The other symbols used have their usual meaning. The system (4.1) discretized in the most straightforward way, e.g., on the B grid, has the form

$$\frac{\partial u}{\partial t} = -g\delta_x \overline{h}^y + fv, \quad \frac{\partial v}{\partial t} = -g\delta_y \overline{h}^x - fu,$$

$$\frac{\partial h}{\partial t} = -H(\delta_x \overline{u}^y + \delta_y \overline{v}^x). \qquad (4.2)$$

In (4.2), the symbol δ and the overbar, respectively, represent the simplest two-point centered differencing and averaging operators applied in the direction indicated by the accompanying subscript or superscript. Following Janjic (1984), the velocity components on the B grid may be written in terms of the velocity potential χ and the stream function ψ in the form

$$u = \delta_x \overline{\chi}^y - \delta_y \overline{\psi}^x, \quad v = \delta_y \overline{\chi}^x + \delta_x \overline{\psi}^y. \quad (4.3)$$

Then, after substituting the expressions (4.3) into the system (4.2), and rearrangement, one obtains

$$\frac{\partial \chi}{\partial t} = -gh + f\psi, \quad \frac{\partial \psi}{\partial t} = -f\chi,$$

$$\frac{\partial h}{\partial t} = -H(\delta_{xx}\overline{\chi}^{yy} + \delta_{yy}\overline{\chi}^{xx}), \qquad (4.4)$$

where repeated subscripts and superscripts indicate repeated applications of the operators they are accompanying. As can be seen from (4.4), the only possible reason for the B grid problems is the insufficiently accurate computation of the Laplacian due to the averaging of the derivatives of the velocity potential χ in the continuity equation. An inspection of the finite difference equations (4.4) reveals that they are defined on a nonstaggered grid, carrying all three variables χ, ψ and h at each grid point (Janjic 1984). This type of grid is also shown in Fig. 3. It was named Z grid by Randall (1994). Thus, the B grid, together with the definitions (4.3), is equivalent to the Z grid (Gavrilov, 2004). However, there is an important difference between the simulation of the gravity-inertia wave propagation on the grids B and Z. On

the Z grid, the continuity equation can be written in the form

$$\frac{\partial h}{\partial t} = -H(\delta_{xx}\chi + \delta_{yy}\chi), \qquad (4.5)$$

without the averaging in the divergence term that was responsible for the B grid problems. However, an application of the Z grid in case of more complex equations would require costly conversions between the velocity components and the velocity potential and the stream function. A more complete comparison of the properties of the remaining two possibilities, the staggered grid C and the semi-staggered grids B and E can be found, e.g., in Janjic and Mesinger (1984, 1989). These considerations, however, do not give decisive advantage to either of the two choices. The problems on the semi-staggered grids B and E are restricted mainly to the shortest waves, while in the case of the slow internal modes, and/or weak stability, the C grid may develop problems in the entire range of the admissible wave numbers (Arakawa and Lamb, 1977). In addition, there is an effective technique for filtering the low frequency, short-wave noise resulting from the inaccurate computation of the divergence term on the semi-staggered grids (Janjic, 1979). More sophisticated, nondissipative methods ("deaveraging" and "isotropisation") for dealing with the problem also have been proposed (Janjic et al., 1998), leading to dramatic improvements of the finite-difference frequencies of the short gravity-inertia waves on the semi-staggered grids.

The results discussed so far are relevant for classical synoptic scale models. In order to address the question of the choice of the horizontal grid as the mesoscales are approached, the linearized anelastic nonhydrostatic system is a better starting point than the linearized shallow water equations (4.1) (communicated by Klemp, 1997; Janjic, 2003). As before, the problems with the anelastic system on the B grid are mainly due to the averaging within the divergence term, and on the C grid mainly due to the averaging of the Coriolis force. For example, if the ratio between the horizontal grid size and the vertical grid size is 30, $f = 0.0001$, the Brunt-Vaisala frequency is $N = 0.0001$, and the

wavelength in the vertical is 32 grid intervals, the true relative frequency v/f, and the relative frequency on the B grid, are both equal to unity throughout the admissible wave number range. On the other hand, as can be seen from Fig. 4, with the same values of the parameters, the relative frequency on the C grid is not a constant. This leads to a nonzero group velocity throughout the admissible wave-number range, including the longest waves. For more details concerning this example, the reader is again referred to Janjic (2003).
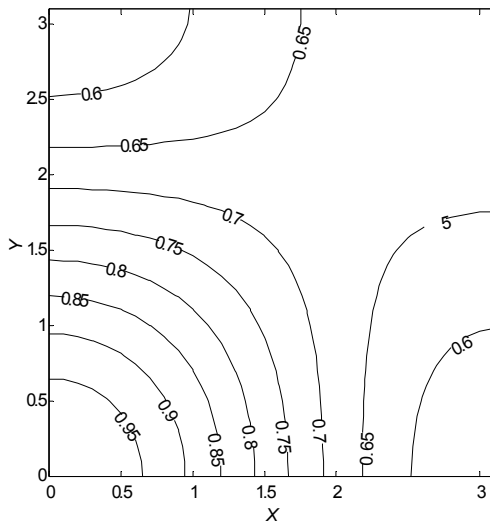

Fig. 4. The ratio v_C/f as a function of wave number.

On the other hand, the example shown in Fig. 5 indicates how bad the problem can be on the B grid. The two 24 hour sea level pressure forecasts shown in the figure were computed using 30 *km* horizontal resolution and very light dissipation. The contour interval was set to 1 *hPa* in order to emphasize the noise that might develop. The forecast in the upper panel was obtained doing nothing to alleviate the B grid problem, while the forecast in the lower panel was obtained using well converged "deaveraging" (Janjic et al., 1998) which substantially improves the frequencies of the gravity-inertia waves on the B grid. As can be seen comparing the forecasts in the upper panel and in the lower panel, the presence of the problem cannot be visually detected. The forecast in the upper panel generally is not noisier than the forecast in the lower panel. This result appears to be
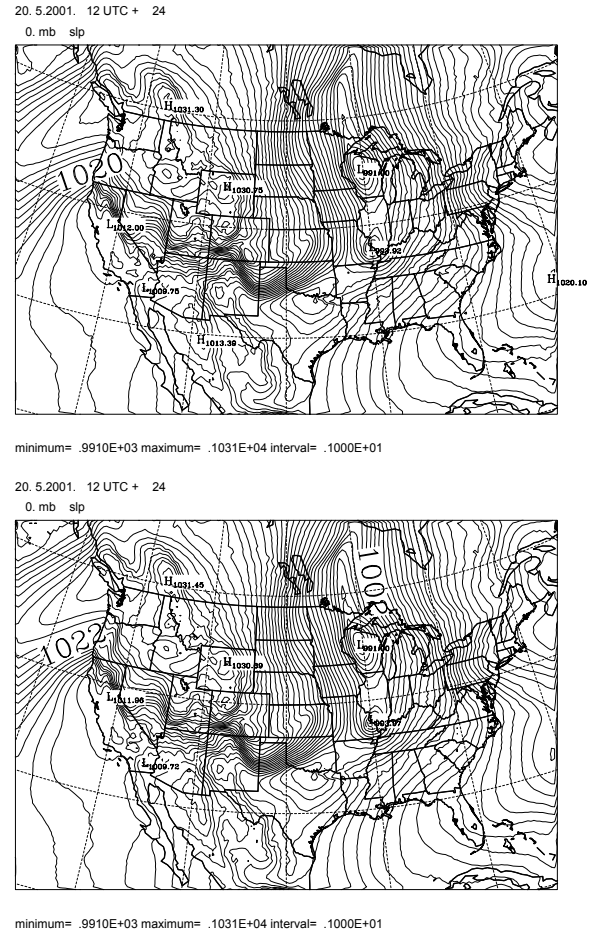

Fig. 5. Examples of 24 hour forecasts of the sea level pressure on the B grid without any control of the grid separation problem (upper panel) and with deaveraging (lower panel). The contour interval is 1 *hPa*.

in conflict with an earlier result (Janjic, 1979). However, in the earlier test the horizontal resolution was 160 *km*, so that the advection had a lesser effect in providing communication between the grid points than in the current test with the 30 *km* resolution.

Since the problems on the semi-staggered grid B are restricted to the shortest resolvable scales, and they are less sensitive to the stability and the choice of the vertical and horizontal grid sizes, the preference was given to the semi-staggered grids. For historical reasons, the E grid is used in the initial version of the NCEP Nonhydrostatic Meso model, although a B grid version (NMM-B) with identical properties also exists (Janjic, 2003).

The longitude-latitude coordinates are rotated in the model in such a way that the

coordinate origin is located in the middle of the integration domain. In this way, the reduction of the longitudinal grid-size is minimized as the southern and the northern boundaries of the integration domain are approached, and, therefore, longer time steps can be used.

5. VERTICAL COORDINATE AND VERTICAL STAGGERING

By far the most widely used method for representing topography are terrain following coordinates such as the sigma coordinate (Phillips, 1957), or its extensions such as the hybrid sigma-pressure coordinate of Arakawa and Lamb (1977), or the hybrid eta coordinate of Simons and Burridge (1981). A rare exception has been the step-mountain blocking used in the NCEP Meso (Eta) model. This technique was originally proposed by Bryan (1969), and subsequently widely used in oceanography. Mesinger et al. (1988) implemented this technique in a sigma coordinate atmospheric model. Yet another approach coming from oceanography is the shaved cell method (e.g. Adcroft et al. 1997). Steppeler et al. (2002) reported a successful application of this approach in the dynamics of the Local Model (LM) of the German Weather Service.

The advantage of the step-like mountain blocking is that the coordinate surfaces are quasi-horizontal. This, however, is not without consequences. For example, internal discontinuities are introduced at the vertical sides of the steps that replace the mountain slopes, and lateral boundary conditions are required at these discontinuities. The formal accuracy of the finite-differences at the points next to the internal boundaries is reduced to the first order. In addition, if the no slip boundary conditions are used in order to preserve the major favorable features of the finite-differencing schemes (Janjic, 1977, 1979, 1984), a nonphysical sink of momentum is introduced. Yet another problem is the representation of the physical processes in the surface layer and the planetary boundary layer (PBL). If one wants to represent these processes in a reasonably uniform way throughout the integration domain, including both low-lying and elevated terrain, an approximately equidistant spacing of the vertical levels is required in the lower few kilometers of the atmosphere. However, the vertical resolution needed in order to achieve this goal is still too high. In addition, several recent studies (Adcroft et al, 1997; Gallus, 2000; Gallus and Klemp, 2000; Janjic and DiMego, 2001; Gavrilov, 2002) indicate that more problems should be expected at higher resolutions.

The shaved cell approach has problems associated with complex lower and internal boundary conditions. In addition, as with the step-mountains, the vertical resolution is reduced over elevated terrain which poses additional problems for physical parameterizations.

Thus, despite of all its imperfections, the terrain-following hybrid pressure-sigma vertical coordinate (Arakawa and Lamb, 1977) has been chosen as the best compromise (Janjic, 2003). With the hybrid coordinate, the coordinate surfaces are flat above and away from the mountains. Over the mountains the hybrid coordinate has increased vertical resolution, and the equations are continuous, without the computational internal boundary conditions. Since the hydrostatic pressure is currently used as the vertical coordinate above 400 *hPa*, the possible inaccuracies due to the sloping coordinate surfaces are restricted only to about the lower half of the mass of the atmosphere. Note that, generally, largest errors in the sigma coordinate occur in the stratosphere. Thus, with the hybrid coordinate, the most serious problems associated with the sloping sigma surfaces are eliminated. In addition, the increased resolution presumably acts in the direction of reducing the computational inaccuracies, and certainly improves the representation of the vertical structure of the PBL over elevated terrain.

The usual, Lorenz vertical staggering of the variables is used in the vertical (Janjic, 1977). The geopotential and the nonhydrostatic pressure are defined at the interfaces of the layers, while all three velocity components and temperature are carried in the middle of the model layers. The vertical velocity is defined at the E grid mass points.

6. SPATIAL DISCRETIZATION

The basic discretization principles applied in the NMM, and thoroughly tested in NWP applications in its hydrostatic predecessors the Eta and the HIBU models, have been (Janjic, 1977, 1984):

● Conservation of selected integral properties, and in particular, following Arakawa, the control over the nonlinear energy cascade by the conservation of energy and enstrophy in case of nondivergent flow;
● Cancellation of the contributions of the pressure gradient force and the $\omega\alpha$ term of the thermodynamic equation to the total energy generation, and consequently consistent transformation between the kinetic and potential energy; and
● Minimization of the errors due to sloping sigma surfaces.

Although designed following the same general principles, the specific numerical schemes employed evolved significantly over time and over about two orders of magnitude in horizontal resolution. For example, the problem of the sloping sigma surfaces was first addressed by using the Janjic (1977) method for minimization of the pressure gradient force errors, then by the step-mountain blocking (Mesinger et al., 1988) in the Eta model, and finally by the already discussed hybrid pressure-sigma coordinate (Arakawa and Lamb, 1977) in the NMM. The treatment of the $\omega\alpha$ term has certainly played an important role in the treatment of orography as well (Janjic, 1977). Yet, perhaps the most significant upgrade was the introduction of the new schemes for calculating the contribution of the nonlinear advection terms and the horizontal divergence operators (Janjic, 1984). In the current model formulation, all divergence operators are computed using the fluxes between each point and its eight nearest neighbors. This, "isotropic", divergence operator is used in the Arakawa Jacobian, but also in the hydrostatic continuity equation in order to compute the divergence of mass. Properties of the momentum advection scheme were examined in more detail by Gavrilov and Janjic (1989).

In the case of rotational flow and cyclic boundary conditions, the scheme for horizontal advection of momentum on the E grid conserves the following properties:

- Enstrophy as defined on the staggred grid C (i.e. using the most compact second-order approximation of the Laplacian in order to compute vorticity),

$$\sum_{i,j}(\delta_{x'x'}\psi + \delta_{y'y'}\psi)^2 \Delta A, \qquad (6.1)$$

- Rotational kinetic energy as defined on the staggered grid C,

$$\sum_{i,j}\frac{1}{2}(\delta_{y'}\psi)^2 \Delta A + \sum_{i,j}\frac{1}{2}(\delta_{x'}\psi)^2 \Delta A, \qquad (6.2)$$

- Rotational momentum as defined on the staggered grid C,
- Rotational kinetic energy as defined on the semi-staggered grid E,

$$\sum_{i,j}\frac{1}{2}[\delta_y\psi^2 + \delta_x\psi^2]\Delta A, \qquad (6.3)$$

- Rotational momentum as defined on the semi-staggered grid E.

The Z grid equivalent of the E grid used to define the quantities (6.1)-(6.3) is shown in Fig. 6 together with the orientation of the coordinate axes x,y and x',y' appearing in
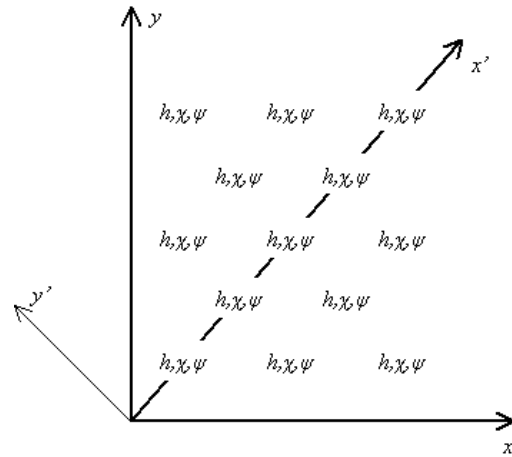

Fig. 6. The Z grid equivalent of the E grid. Orientations of the coordinate axes x,y and x',y' are indicated.

(6.1)-(6.3). As before, φ and ψ are the velocity potential and the stream function, respectively, and h stands for mass point variables. The symbol ΔA denotes the area of the grid boxes, and the summation sign with the subscripts i,j represents the summation in the horizontal.

In case of general flow, the scheme conserves:

- Kinetic energy as defined on the semi-staggered grid E

$$\sum \frac{1}{2}[(\delta_x\varphi - \delta_y\psi)^2 + (\delta_y\varphi + \delta_x\psi)^2]\Delta V , \quad (6.4)$$

- Momentum as defined on the semi-staggered grid E.

In (6.4), the summation sign indicates the summation over all grid points, and the symbol ΔV denotes the grid box volume in hydrostatic vertical coordinates. The scheme for horizontal advection of temperature also conserves the first and the second moments of temperature.

Two options are available in the model for dealing with the problem of the semi-staggered grids with the frequencies of the short gravity-inertia waves. The first one is the selective filtering technique developed by Janjic (1979). The second one is the deaveraging technique proposed by Janjic et al. (1998). The deaveraging is computationally very efficient and requires only few simple iterations on the hydrostatic pressure tendency. Although the deaveraging is non-dissipative, and therefore physically better founded, the dramatic improvement of the frequencies of the shortest gravity-inertia waves achieved on the semi-staggered grids requires that the time step be significantly reduced which leads to reduced computational efficiency of the model. Thus, it is not obvious which of the two options should be given preference in practical NWP applications, particularly in the light of the situation shown in Fig. 5.

Concerning the vertical discretization of the basic dynamical variables, quadratic conservative vertical advection is used. In addition to the material surface boundary conditions requiring that the total derivative of the vertical coordinate (vertical velocity) be equal to zero at the top and at the bottom of the model's atmosphere, vertical boundary conditions are needed also for the nonhydrostatic deviation of pressure. It is assumed that the nonhydrostatic pressure deviation vanishes at the top of the atmosphere, while its vertical derivative vanishes at the bottom (Janjic et al., 2001).

The centered conservative schemes used for advection of the basic dynamic variables develop well known problems in case of advection of positive definite scalars with large spatial variation, such as specific humidity, cloud water, or turbulence kinetic energy. For this reason, an upgraded version of the scheme used for advection of passive substances in the NCEP Eta model (Janjic, 1997) is applied. The scheme consists of three steps. In the first step an upstream biased scheme is used to advect the passive substance. In the second step, antifiltering is applied, with antifiltering parameters optimized in such a way as to minimize computational dispersion in sheared flows. Finally, in the third step, forced conservation of the advected quantity is imposed. The scheme appears to be a reasonable compromise between the requirements for accuracy and computational efficiency.

7. TIME DIFFERENCING

Following again the same proven principles for discretization in time as in its hydrostatic predecessors (Janjic, 1979), the hydrostatic core of the equations (2.3)-(2.7) used in the NMM is split into the following two subsystems (Janjic et al., 2001; Janjic, 2003)

$$(\frac{\partial \mathbf{v}}{\partial t})_i = -\nabla_\sigma \Phi - \alpha \nabla_\sigma \pi + f\mathbf{k} \times \mathbf{v} \quad (7.1)$$

$$(\frac{\partial T}{\partial t})_i = \frac{\alpha}{c_p}[\mathbf{v} \bullet \nabla_\sigma \pi - \int_0^\sigma \nabla_\sigma \bullet (\mu\mathbf{v})d\sigma'] \quad (7.2)$$

$$(\frac{\partial \mu}{\partial t})_i + \nabla_\sigma \bullet (\mu\mathbf{v}) + \frac{\partial(\mu\dot{\sigma})}{\partial \sigma} = 0 \quad (7.3)$$

$$\left(\frac{\partial \mathbf{v}}{\partial t}\right)_{ii} = -\mathbf{v}\nabla_\sigma \mathbf{v} - \dot{\sigma}\frac{\partial \mathbf{v}}{\partial \sigma} \qquad (7.4)$$

$$\left(\frac{\partial T}{\partial t}\right)_{ii} = -\mathbf{v}\bullet\nabla_\sigma T - \dot{\sigma}\frac{\partial T}{\partial \sigma} \qquad (7.5)$$

The time derivatives of the subsystems (7.1)-(7.3) and (7.4)-(7.5) are denoted by the subscripts *i* and *ii,* respectively. The two subsystems are solved using different time stepping methods. Note that the splitting is not done by separating automatically all the advection terms. Namely, the system with subscripts *i* includes the advection of pressure in the omega-alpha term of the thermodynamic equation. The contribution of this term compensates the kinetic energy production by the pressure gradient force in the total energy equation. As can be readily verified, due to the presence of this term, the system (7.1)–(7.3), conserves energy. The system (7.4)–(7.5) also conserves energy, except for the changes due to the redistribution of mass.

An economical forward–backward scheme (Ames, 1969; Gadd, 1974; Janjic and Wiin–Nielsen, 1977; Janjic, 1979) has been used for the system (7.1)–(7.3). The properties of the scheme used in the model were examined in the case of the linearized shallow water equations by Janjic and Wiin–Nielsen (1977) and Janjic (1979). Concerning the contributions of the horizontal advection terms in (7.4)–(7.5), historically, the additively split, iterative, first–forward–then–(slightly off–) centered time differencing scheme has been applied with time steps twice longer than those used to solve the subsystem (7.1)–(7.3) in the HIBU and the Eta models (Janjic, 1979). The Matsuno scheme has been used in a similar way for the vertical advection terms in (7.4)–(7.5). This combination has worked very well in the hydrostatic models on the synoptic scales (Janjic et al., 1995). However, in the nonhydrostatic model, two-grid-interval noise in time developed with this time stepping scheme at high resolutions (Janjic, 2003). For this reason, the two–step iterative scheme for horizontal advection has been replaced by the Adams–Bashforth scheme using the short time step. The Adams–Bashforth scheme allows about the same computational efficiency as the two–step, iterative scheme with twice longer time steps, and the accuracy is improved. However, somewhat more memory is needed in order to store some of the variables at the third time level, and the physical mode of the Adams–Bashforth scheme is weakly unstable. This instability can be tolerated if the time steps are not too long, or eliminated by a very slight off-centering which preserves the second order accuracy. Note that large ratios between the advection time step, and the time step used for the remaining terms of the equations cannot be used in NWP applications. This ratio is restricted to only about 2 on the semi-staggered grids, where longer short steps can be used than those allowed by the CFL criterion on the staggered grid C.

The trapezoidal scheme for the Coriolis force terms has been also replaced by the Adams-Bashforth scheme. The reason for this change was the possibility of overestimating the amplitude of the divergent part of flow with the trapezoidal scheme (Janjic and Wiin-Nielsen, 1977).

For the vertical advection, the Matsuno scheme has been replaced in later versions of the NMM by the unconditionally stable Crank-Nicholson scheme. Namely, as a legacy from the Eta model which required very high vertical resolution in order to resolve the processes over elevated terrain, the NMM is often run with higher vertical resolution than necessary with the hybrid pressure-sigma coordinate, so that the vertical advection sometimes dangerously approaches the limit imposed by the CFL criterion.

For simplicity, the time differencing has been presented using only the hydrostatic part of the model dynamics. The treatment of the contribution of the nonhydrostatic dynamics is more involved, and more details on the time stepping procedures used can be found in Janjic et al. (2001) and Janjic (2003). A novelty in the treatment of the nonhydrostatic terms is that the iterative method for solving the vertical implicit pressure equation discussed in Janjic et al. (2001) has been replaced by a direct solver. This modification has brought a visible further improvement of the computational efficiency of the model. Currently, the flux correction passive

substance transport remains the single most expensive part of the model dynamics.

8. THE NONLINEAR DYNAMICS OF THE NMM

Nastrom and Gage (1985) examined measurements made by commercial aircraft and found that one-dimensional kinetic energy spectra along their flight-paths in the lower stratosphere and in the upper troposphere follow the −5/3 slope in the range from several hundred kilometers to several kilometers. Several possible explanations for this spectral shape have been proposed (e.g. Gage, 1979; Lilly, 1983; Gage and Nastrom, 1986; Tung and Orlando, 2003). They include the downscale nonlinear energy cascade and an inverse cascade from smaller to larger scales.

The statistical properties of atmospheric spectra typically are investigated in extended integrations (tens or hundreds of days), and the spectra are averaged over long periods (tens or hundreds of days) in order to ensure that statistical equilibrium is reached. The need for extended integrations and long averaging periods arise due to the time scale of the nonlinear cascade. In addition, the size of integration domain in mesoscale runs is typically smaller than the size of the large-scale atmospheric disturbances that feed the downscale nonlinear cascade. Thus, it appears that physical or spurious sources of energy other than the downscale nonlinear cascade from the large-scale motions are needed in order to develop and maintain the −5/3 spectra in mesoscale atmospheric models. Such sources may be (a) physically justified mesoscale forcing, (b) early collapse of the spectrum due to spurious computational nonlinear cascade, (c) other small-scale computational errors such as the errors due to the representation of topography, etc.

It should be noted that the WRF NMM and the NMM-B are well qualified for investigating atmospheric spectra. They conserve energy and enstrophy, which generally improves the accuracy of the nonlinear dynamics. In particular, the energy and enstrophy conservation controls the nonlinear energy cascade and restricts an early spurious energy transfer toward smaller scales by nonlinear interactions. The energy conservation improves the stability of the

model and eliminates the need for excessive dissipation (either explicit or built into the finite-difference schemes) that could affect the spectra generated by the model. In addition, the WRF-NMM and the NMM-B use hybrid pressure-sigma vertical coordinate, so that, except for the errors propagating from below, in the upper troposphere and in the stratosphere they are free of the sigma coordinate errors that are largest at higher altitudes. Finally, explicit formulation of major dissipative processes allows precise "dosage" of dissipation.

The time averaged spectrum over forecast hours 36-48 at 300 hPa (blue diamonds) obtained in the WRF NMM run in the East domain for the case of hurricane Isabel (initial data September 17, 18Z, from the Eta data) with the resolution of 8 km and 60 levels is shown in Fig. 7. The −3 (purple squares) and −5/3 (yellow triangles) slopes are also shown for comparison. As can be seen from the figure, the spectrum spun up by the model.
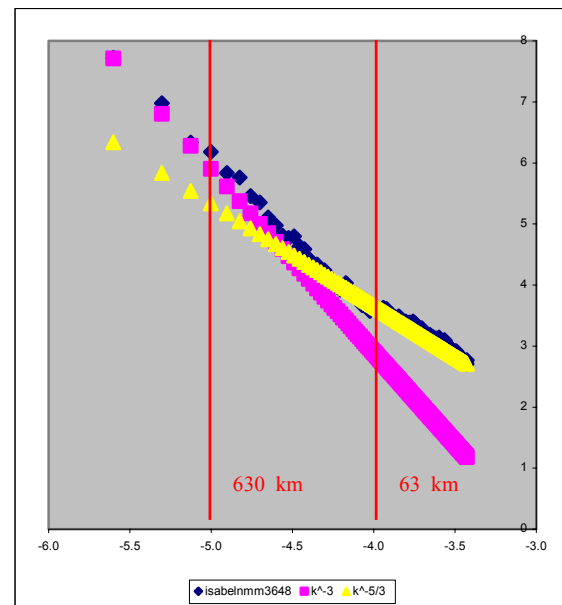

Fig. 7. Time average over 36-48 hours of the WRF NMM spectra (blue diamonds) at 300 hPa in the East domain. The −3 (purple squares) and −5/3 (yellow triangles) slopes are shown. Run starting from 18Z, 09/17/2003 (Isabel), Eta data, 8 km, 60 levels resolution.

agrees remarkably well with the observed Nastrom and Gage (1985) spectrum.

The time averaged spectrum over forecast hours 36-48 at 300 *hPa* (blue diamonds) obtained in a NMM B run over Atlantic is shown in Fig. 8. The −3 (purple squares) and −5/3 (yellow triangles) slopes are again shown for comparison. The NMM B was run using the resolution of 15 *km* in the horizontal and 32 levels in the vertical in a domain of the
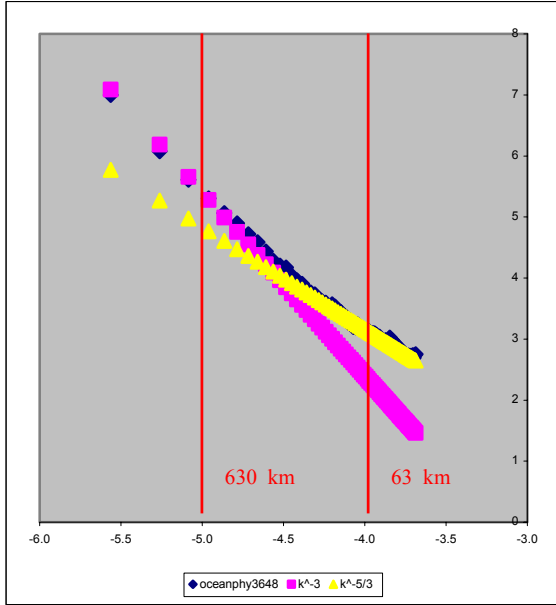

Fig. 8. Time average over 36-48 hours of the NMM B spectra (blue diamonds) at 300 *hPa* over Atlantic. The −3 (pink squares) and −5/3 (yellow triangles) slopes are shown. Run starting from 12Z, 09/07/2003, GFS data, 15 *km*, 32 levels resolution.

same size as the East domain. As can be seen from the figure, an excellent agreement between the simulated and the observed spectrum was again achieved.

As expected on the basis of theoretical considerations, the presented results demonstrate that the nonlinear dynamics used in the NMM have been successful in reproducing the observed mesoscale atmospheric spectra, even at a rather modest resolution of 15 *km*. However, whether the energy in the small-scale part of the spectrum comes from legitimate physical sources is an issue that requires further investigation. In other words, there is no guarantee that the model produced −5/3 spectrum is generated by the same mechanisms as the Nastrom and

Gage −5/3 spectrum observed in nature. On the positive side, one could argue that the nonlinear dynamics still performed well generating the −5/3 spectrum no matter what was the source of energy.

An interesting question is also how the NMM nonlinear dynamics reproduce the energy spectrum in the case of three-dimensional turbulence. In order to address this problem, the NMM B was run with horizontal resolution of 1 *km*, and an average vertical resolution of about 500 *m*. The horizontal domain had 112 by 112 points. Double periodic boundary conditions were specified along the lateral boundaries. The model was initialized with the vertical thermodynamic structure of the Fort Sill storm of May 20, 1977, and the initial wind field was set to zero. The spectrum of w^2 at the 700 *hPa* level corresponding to decaying turbulence generated by moist convection was obtained by averaging the spectra between forecast hours 3 and 4. The time averaged spectrum (blue diamonds) is shown in Fig. 9.
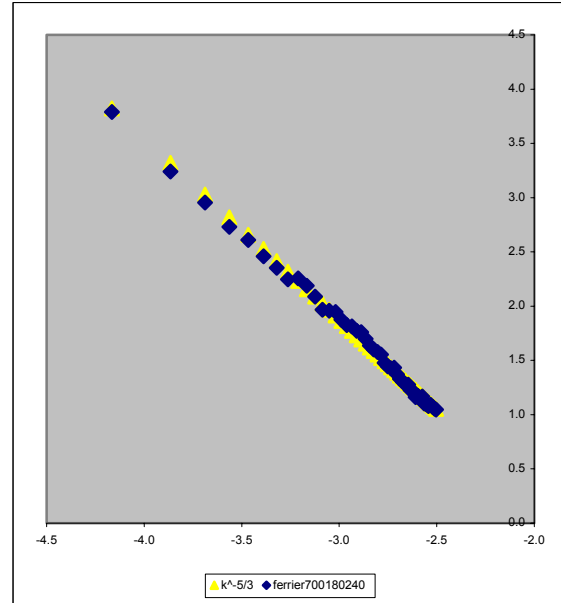

Fig. 9. Decaying 3D turbulence. Time average over hours 3-4 of the NMM B spectra of w^2 (blue diamonds) at 700 *hPa* in a domain with double periodic boundary conditions.

For comparison, the −5/3 slope (yellow triangles) is also shown. As can be seen from the figure, the agreement between the

computed and the theoretical spectrum is again almost perfect.

9. OPERATIONAL APPLICATIONS AND EXPERIMENTAL RUNS

Since July 2002, the NMM has been run operationally in NCEP High Resolution windows in six nested domains (West, Central, East, Alaska, Hawaii, Puerto Rico) shown in Fig. 10. The horizontal resolution is 8 *km* for all domains except for the Alaska domain where the horizontal resolution is 10 *km*. The model has 60 unequally spaced levels in the vertical. In addition, the model is used for fire weather forecasting and other purposes on call.
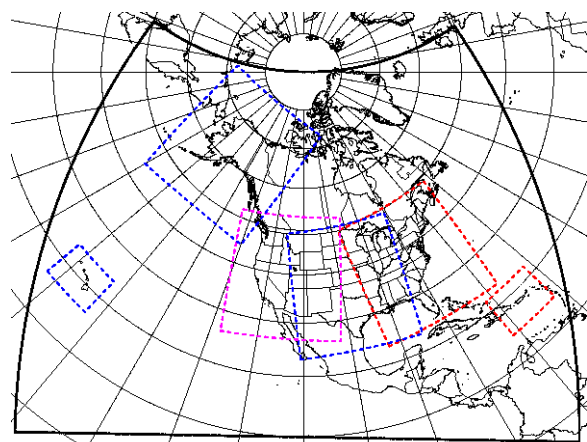

Fig. 10. The six High Resolution Windows: West, Central, East, Alaska, Hawaii and Puerto Rico embedded into the Eta domain (solid black line).

The model topography is defined as unfiltered gridbox means of 30'' USGS Digital Elevation Model data. Although unfiltered topography introduces forcing at the smallest resolvable scales that can adversely affect e.g. the precipitation forecasts, this choice was made hoping that realistic topography will result in better forecasts of low-level flow.

The model does not have its own dedicated data assimilation system. The initial and boundary conditions are defined by interpolation of the operational Meso (Eta) model data. The Meso (Eta) model is run with 12 *km* resolution and 60 levels in the vertical.

In the two small domains the model is run twice a day (Hawaii cycles 00Z and 12Z, Puerto Rico cycles 06Z and 18Z). In the remaining four domains, the model is run once a day starting from 00Z (Alaska), 06Z (West), 12Z (Central) and 18Z (East). The forecasts are computed up to 48 hours.

The computational efficiency of the model has been very high, and substantially higher than the computational efficiency of most nonhydrostatic models. Moreover, further significant improvement of the computational efficiency of the model is possible. The model has been highly reliable and there have been no failures since it began running operationally in July 2002.

In terms of performance on the synoptic scales, generally, the model has been highly competitive with mature operational high-resolution NWP models, despite the fact that it has been handicapped by inconsistent initial and boundary conditions taken from the Eta model, relatively small integration domains, and insufficient tuning of the physical package. Thus, although it is difficult to compare directly the performance of the NMM to that of the Eta model, statistical scores and numerous examples (Black et al., 2002, Janjic et al. 2003) indicate that the NMM adds value to the forecasts of the Eta model. This applies particularly to the details of the flow over complex terrain.

For example, consider the 42 hour forecasts of 10 *m* wind for the Santa Barbara area, California, valid at 00Z, February 6, 2003 that are shown in Fig. 11 (courtesy of Tom Black). The forecast obtained using the 12 *km* Eta model is shown in the upper panel, and the forecast from the 8 *km* NMM West domain run is shown in the lower panel. The bold arrows represent the observations. As can be seen from the figure, generally, there is a much better agreement between the NMM forecast and the observations. In particular, the northeast low level jet that turns to east and southeast over the ocean in the Oxnard area is realistically reproduced in the NMM forecast, while it is completely missing in the Eta forecast.

On the other hand, as shown in Fig. 12 (courtesy of Eric Rogers), the most dramatic differences between the Eta model and the NMM can be seen in vertical structures developing due to the effects of topography. The panels in the column on the left are from the 12 *km* Eta run, and the panels in the

column on the right are from the NMM Eastern domain run. The middle and bottom panels of the two columns represent 12 hour
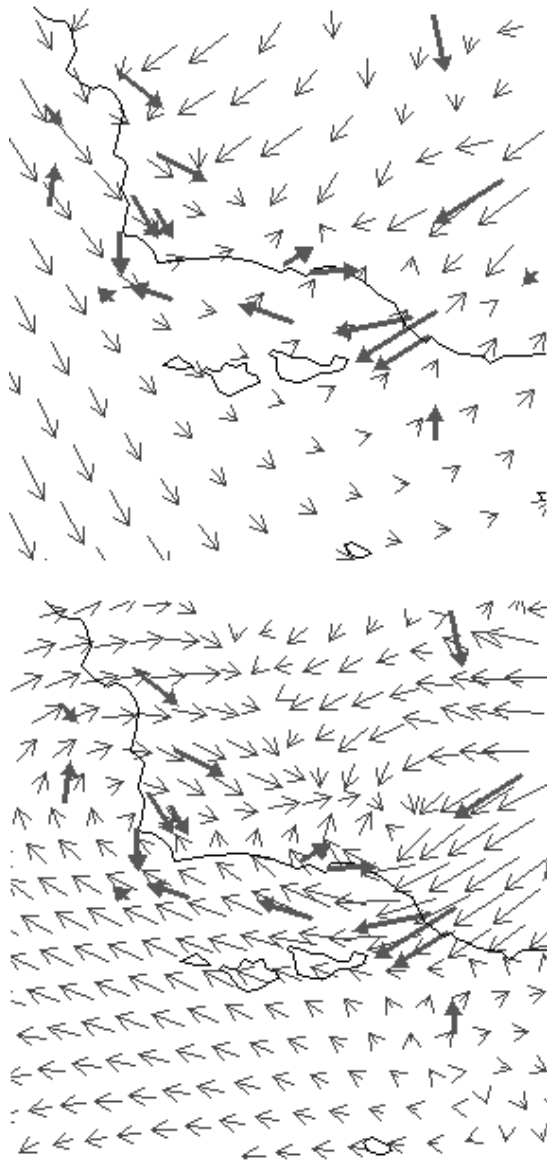

Fig. 11. The 42 hour forecasts of 10 m wind for the Santa Barbara area, California, valid at 00UTC, February 6, 2003. The forecast obtained using the 12 *km* Eta model is shown in the upper panel, and the forecast from the 8 *km* NMM West domain run is shown in the lower panel. (Courtesy of Tom Black)

and 15 hour forecast cross sections, respectively, starting from 18Z, January 7, 2003. The cross sections are taken along the blue lines in the top panels. The topography is indicated in the top panels by color shading

with the contours at 100, 175, 250, 375, 500, 750, 1000, 1250 etc. meters, and by the shaded area at the bottom of the cross sections. The blue and brown contour lines indicate the negative (upward) and positive (downward) vertical velocity $\omega = dp/dt$, respectively. The contour interval is 0.2 $Pa\ s^{-1}$. The potential temperature is represented by the dashed red contour lines with the contour interval of 4 degrees. The background color shading in the cross sections represents isotachs with the contour interval of 10 *Knts*.

As can be seen from the figure, the vertical motions are much stronger in the NMM than in the Eta model. Moreover, the wave length of the mountain waves in the NMM is much shorter than in the Eta model. Also, the effect of vertical transport of momentum is visible in bottom panels, particularly in the case of the NMM. In addition to resolution, the representation of mountains and the nonhydrostatic dynamics are believed to have played a role in producing so different results.

An experimental 12 hour forecast of the sea level pressure starting from September 17, 2003, 12Z is shown in Fig. 13. This forecast covers a part of the life cycle of the tropical storm Isabel. The NCEP GFS data were used to specify the initial and boundary conditions for the NMM. As can be seen from Fig. 13, the predicted pressure in the center of the storm was 951.72 *hPa*, while the observed value at that time was 953 *hPa*. The 30 hour forecast of the accumulated 3 hour precipitation for this case is shown in Fig. 14. The landfall occurred at about this forecast time, and, as can be seen from Fig. 14, it was rather accurately predicted by the model.

These examples demonstrate that the NMM has the ability to spin up and maintain realistically deep tropical storms and to predict their track with remarkable accuracy. Actually, at the forecast time shown in Fig. 13, as well as at subsequent forecast times (not shown), the predicted tropical cyclone was overdeveloped by several hecto Pascals. Consistent with the slight overdevelopment of the cyclone, the landfall time and the subsequent dissipation of the storm were somewhat retarded. This, however, could have been expected considering that the NMM was run with practically no explicit or implicit lateral diffusion or filtering.
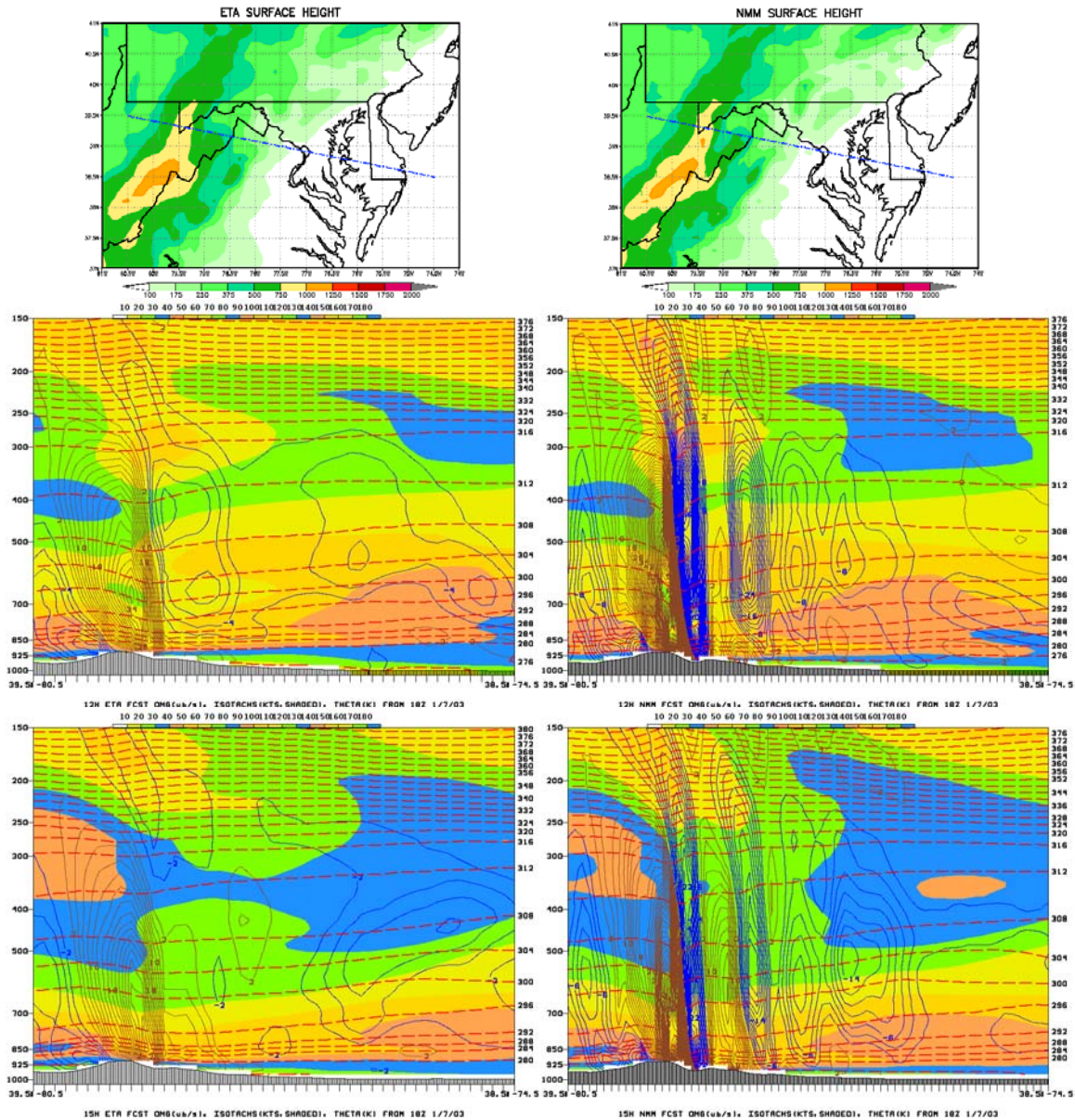
Fig. 12. The 12 *km* Meso (Eta) (left column) and the 8 *km* NMM Eastern Domain (right column) cross sections. The middle and bottom panels are 12 hour and 15 hour forecasts, respectively, starting from 18Z, January 7, 2003. The cross sections are taken along the blue lines in the top panels. The topography is indicated in the top panels by color shading with the contours at 100, 175, 250, 375, 500, 750, 1000, 1250 etc. meters, and by the shaded area at the bottom of the cross sections. The blue and brown contour lines are the negative (upward) and positive (downward) values of vertical velocity $\omega = dp/dt$, respectively. The contour interval is $0.2 Pa\ s^{-1}$. The dashed red contour lines are potential temperature with the contour interval of 4 degrees. The background color shading in the cross sections represents isotachs with the contour interval of 10 *Knts*. (Courtesy of Eric Rogers)
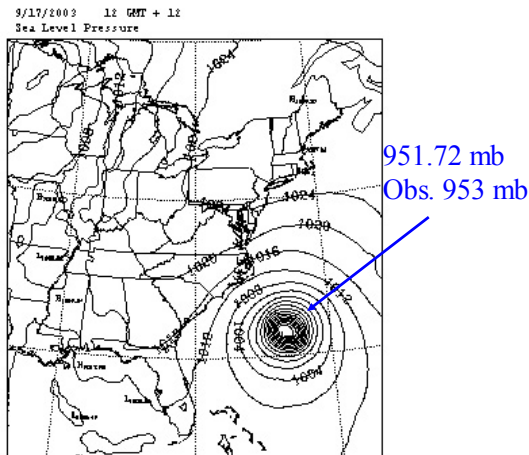
Fig. 13. An experimental 12 hour forecast of the sea level pressure starting from September 17, 2003, 12Z. The NCEP GFS data were used for initial and boundary conditions.
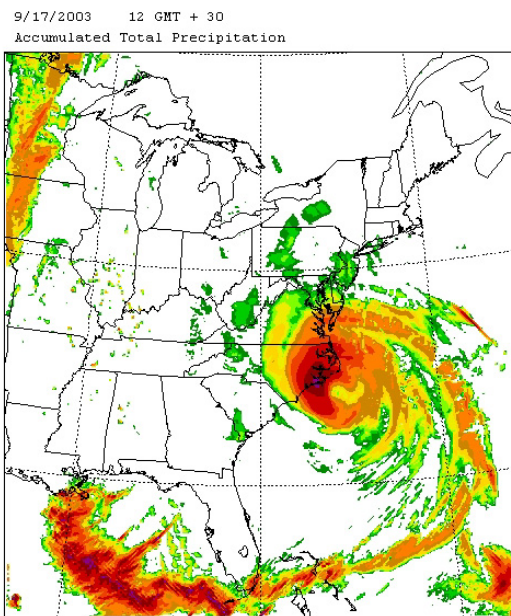

Fig. 14. The 30 hour forecast of the accumulated 3 hour precipitation indicating the location of the landfall. The forecast started at September 17, 2003, 12Z. The NCEP GFS data were used for the initial and boundary conditions.

The example shown in Fig. 15 is from NCEP's experimental runs with 4.5 km resolution that are made in support of the Storm Prediction Center (SPC) Spring

Program. These forecasts are run once a day up to 30 hours ahead starting from 00Z data with disabled cumulus convection parameterization. The 24 hour forecast of accumulated 1 hour precipitation valid at 00Z April 21 is shown in the upper panel of Fig. 15, while the verifying radar reflectivity is shown in the lower panel (Courtesy of Jack Kain). As can be seen from the figure, the predicted precipitation pattern and timing were remarkably similar to the verification.
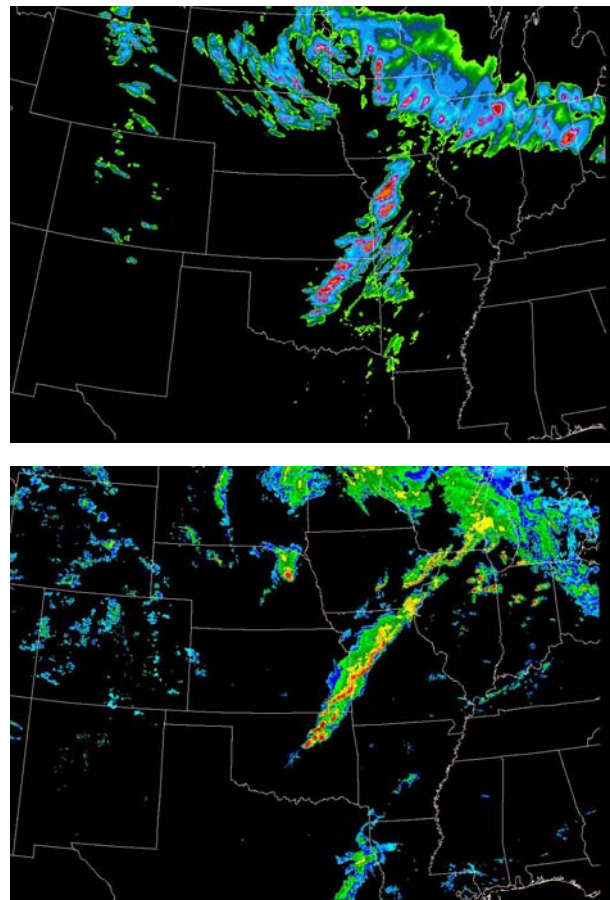

Fig. 15. The 24 hour forecast of accumulated 1 hour precipitation valid at 00Z April 21 (upper panel) and verifying radar reflectivity (lower panel). (Courtesy of Jack Kain)

Finally, results of a recent diagnostic study (http://www-ad.fsl.noaa.gov/fvb/rtvs/wrf/retro_runs/) inspire interesting considerations regarding ensemble forecasting and relative importance of various parts of model formulation for forecasting basic dynamical variables on larger scales. Namely, the vector wind RMS

errors at standard pressure levels averaged over one month of forecasts over the Alaska domain are shown in Fig. 16 for two dynamical cores run with two different physical packages. The two dynamical cores are denoted by WRF NMM and Other, and the two physical packages are denoted by Phys1 and Phys2, respectively. The scores are computed against observations using the NCEP standard verification package. As can be seen from the figure, the blue and red lines corresponding to the errors of the Other dynamical core run with the physical packages Phys1 and Phys2 cluster together, and so do the black and gray lines corresponding to the errors of the WRF NMM dynamical core run with the two physical packages. Apparently, in this case the clustering occurs primarily by the dynamical cores, and not by the physical

packages. Such clustering indicates that it is important to use different dynamical cores in ensemble forecasting systems.

Similarly, the vector wind RMS errors at standard pressure levels averaged over one month of forecasts over the West domain are shown in Fig. 17 for the two dynamical cores and the two physical packages. In addition, the RMS errors of the Eta model are included in the plot. Namely, the topography certainly plays an important role in the West domain, and it is interesting to see whether and how much the method used to represent the topography affects the clustering of the errors. As before, the scores are computed against observations using the NCEP standard verification package. As can be seen from Fig. 17, the results again cluster primarily by the dynamical cores. The blue and red lines
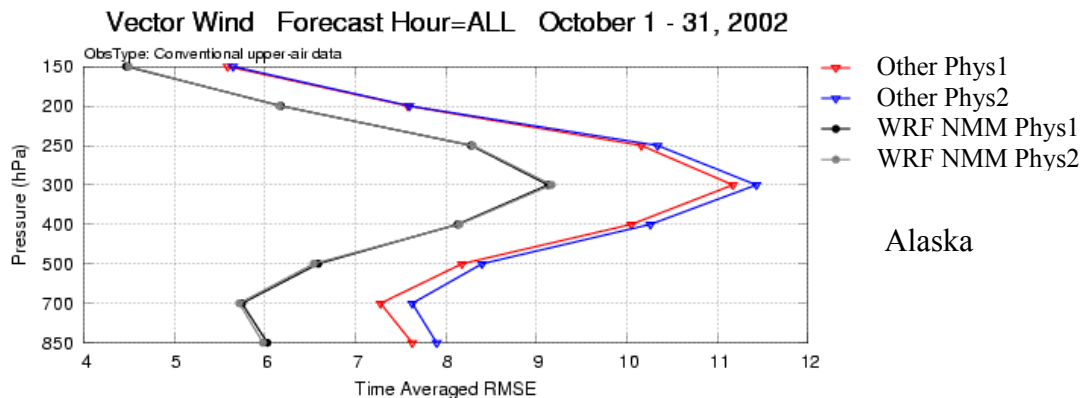

Fig. 16. Vector wind RMS errors at standard pressure levels averaged over one month of forecasts for two dynamical cores run with two different physical packages in the Alaska domain.
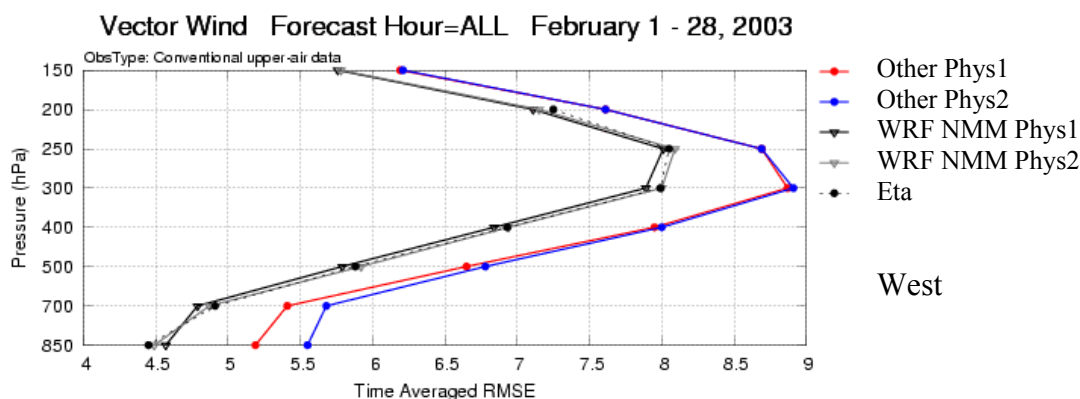

Fig. 17. Vector wind RMS errors at standard pressure levels averaged over one month of forecasts for two dynamical cores run with two different physical packages in the West domain.

corresponding to the Other dynamical core cluster together, and so do the black and gray lines corresponding to the WRF NMM core. However, the Eta errors join the WRF NMM core in this domain, indicating that on larger scales more fundamental differences in the discretization between the Other core and the WRF NMM core are more important for forecasting basic dynamical variables in the free atmosphere than the method used to represent the topography. Of course, as indicated also by some of the preceding examples, the situation is quite different with forecasting the details of the flow over complex terrain, or precipitation and near surface variables. In the latter case, the representation of topography and the physical parameterizations are certainly of utmost importance.

10. SOME RECENT WORK

The convection schemes deserve special attention because of their large impact on precipitation forecasts, and because of concerns about the validity of the assumptions built into their design at the currently used transitional horizontal resolutions. Another issue related to precipitation is that the success of precipitation forecasts has been measured mainly by the equitable threat and bias scores at NCEP, and the equitable threat score favors precipitation forecasts that are considered too smooth by some users. For this reason, producing heavier precipitation with more small-scale details is now considered desirable, even if it would result in somewhat lower threat scores. The current work on the convection attempts to address both of these issues, i.e., the applicability of the convection parameterization at the transitional resolutions, and the lack of details in the precipitation forecasts.

In the deep convection part of the Betts-Miller-Janjic (BMJ) scheme, Janjic (1994) extended the Betts-Miller (Betts 1986) deep convection parameterization *(i)* by introducing a nondimensional parameter representative of the convective regime, and *(ii)* by assuming that the reference profiles and the relaxation time depend on this parameter. Janjic (1994) defined this parameter by

$$E = const \frac{\overline{T} \Delta S}{\Delta P}.$$ (10.1)

and called it cloud efficiency. In (10.1),

$$\Delta S = \sum \frac{c_p \Delta T + L \Delta q}{T} \Delta p ,$$

is the entropy change over the time step,

$$\Delta P = \sum c_p \Delta T \Delta p ,$$

is the precipitation over the time step, and

$$\overline{T} = \frac{\sum c_p (T + \frac{\Delta T}{2}) \Delta p}{\sum \Delta p} .$$

is the mean temperature of the cloud. The symbols p, T and q represent pressure temperature and specific humidity, and the summation is performed from the cloud base to the cloud top.

In the Janjic (1994) deep convection scheme the equilibrium temperature and moisture profiles vary between universal heavy convection profiles based on the Betts (1986) profiles, and the moist adiabat depending on the cloud efficiency. When ΔS, and consequently E, tend to zero, the profiles approach the moist adiabat. In case of large entropy changes the relaxation toward the reference profiles is faster than in the case of more stable stratification closer to the moist adiabat (Janjic, 1994).

In a recent upgrade of the deep convection algorithm, an attempt was made to improve the transition between the convection and the grid-scale precipitation depending on horizontal resolution. Namely, the entropy change measures the stabilization of the convective column. Thus, if the threshold for entropy change needed for the onset of the deep convection is increased with increased horizontal resolution, the instabilities that were handled by the parameterization of convection at coarser resolutions will be treated explicitly at higher resolutions. This modification brought a significant improvement concerning the small-scale structure of precipitation forecasts. However,
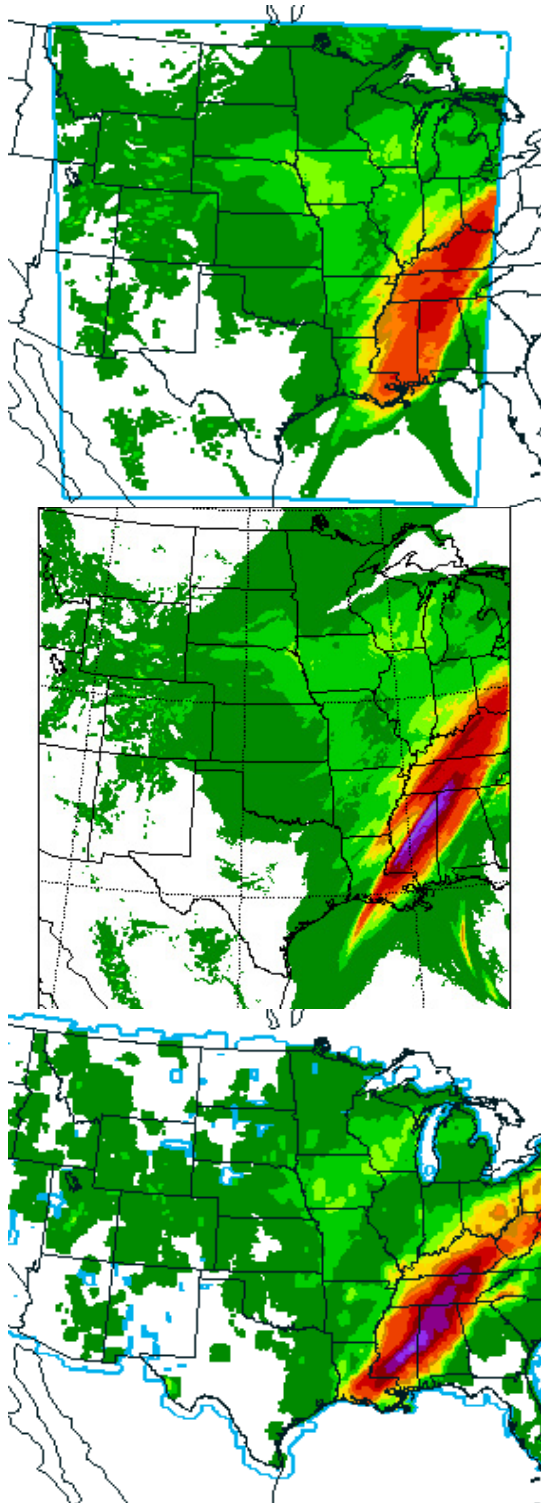
Fig. 18. The operational 24 hour forecast of the 24 hour accumulated precipitation in the Central domain valid at 12Z, February 06, 2004 (top panel), forecast with the modified BMJ scheme (middle panel), and the verification analysis (bottom panel).

taking into account the entrainment during the ascent of the buoyant particle used to estimate the location of the cloud top proved most effective in producing the desired heavy precipitation amounts in the forecast. In addition to these changes, more accurate iterative computation of cloud efficiency has been introduced.

The impact of the described changes is illustrated in Fig. 18. The operational 24 hour forecast of the 24 hour accumulated precipitation in the Central domain valid at 12Z, February 06, 2004, is shown in the top panel. The forecast with the modified BMJ scheme is in the middle panel, and the verifying precipitation analysis is in the bottom panel. As can be seen from the figure, more small scale structure, and a considerably better agreement with the analyzed precipitation amount is obtained using the modified convection.

11. CONCLUSIONS

The NCEP nonhydrostatic mesoscale model (NMM) (Janjic et al., 2001; Janjic, 2003) has been formulated building on the experiences of high resolution hydrostatic numerical weather forecasting. In this way, the favorable features of hydrostatic model formulation are preserved in the range of validity of the hydrostatic approximation.

The basic idea applied was to split the system of the nonhydrostatic equations into two parts: (a) the part that corresponds basically to the hydrostatic system, except for higher order corrections due to the vertical acceleration, and (b) the system of equations that allows computation of the corrections appearing in the first system due to the vertical acceleration. This procedure does not require any linearization or additional approximation.

The nonhydrostatic dynamics is introduced through an add–on module. The separation of the nonhydrostatic contributions shows in a transparent way where, how, and to what extent relaxing the hydrostatic approximation affects the familiar hydrostatic equations. The nonhydrostatic module can be turned on and off, so that the same model can be run in both hydrostatic and nonhydrostatic modes. This allows easy comparison of hydrostatic and nonhydrostatic solutions of

otherwise identical model. This feature also allows that the model be run in the hydrostatic mode at lower resolutions with no extra cost. This is an advantage in case of models designed for a wide range of horizontal resolutions, and in particular for unified global and regional forecasting systems.

At very high resolutions, a two-dimensional version of the model successfully reproduced the classical nonhydrostatic solutions (Janjic et al., 2001). Although such resolutions will not be affordable in NWP applications in the near future, it was necessary to pass these tests in order to demonstrate the soundness of the formulation.

The extra computational cost due to the nonhydrostatic extension is of the order of 20% of the cost of the hydrostatic dynamics. The relatively low cost of the nonhydrostatic dynamics justifies the application of the nonhydrostatic model even at medium resolutions. Compared to the hydrostatic version of the model, no additional computational boundary conditions at the top have been needed in real data runs in a wide range of horizontal resolutions.

The nonlinear dynamics of the NMM model demonstrated the ability to reproduce the observed atmospheric spectrum (Nastrom and Gage, 1985). Moreover, at higher resolution, the NMM successfully reproduced the theoretical spectrum in the case of decaying three-dimensional turbulence excited by moist convection.

The NMM has become operational at NCEP in July of 2002 and has demonstrated a high level of skill. In real data runs, it does not require additional computational boundary conditions at the top.

Despite of application of sophisticated numerical methods, the computational efficiency of the model has been very high, and substantially higher than the computational efficiency of most established nonhydrostatic models. Moreover, further significant improvement of the computational efficiency of the model is possible. This will allow further increase of the resolution and application of more sophisticated physical parameterizations. The model has been highly reliable and there has been no failures since the operations started.

In terms of performance on the synoptic scales, generally, the model has been highly

competitive with mature high-resolution NWP models, despite the fact that it has been handicapped by inconsistent initial and boundary conditions, relatively small integration domain, and almost no retuning of the physical parameterizations. The model demonstrated ability to add value to the forecasts produced by the driving model (the Eta model).

More significant differences between the NMM and the NCEP hydrostatic high resolution Eta model can be seen on smaller scales. The differences are particularly striking in mesoscale vertical structures developed by the two models.

Although the initial results have been very encouraging, further efforts are needed in order to develop full potentials of the model. This applies primarily to retuning of the physical parameterizations.

REFERENCES

Adcroft, A., C. Hill and J. Marshall, 1997: Representation of topography by shaved cells in a height coordinate ocean model. *Mon. Wea. Rev.*, **125**, 2293–2315.

Arakawa, A. and V. R. Lamb, 1977: Computational design of the basic dynamical processes of the UCLA general circulation model. Methods in Computational Physics, 17, Academic Press, 173-265.

Betts, A.K., 1986: A new convective adjustment scheme. Part I: Observational and theoretical basis. *Q. J.R. Meteorol. Soc.*, **112**, 677-691.

Black, T., E. Rogers, Z. Janjic, H. Chuang, and G. DiMego, 2002: Forecast guidance from NCEP's high resolution nonhydrostatic mesoscale model. 15th Conf. on NWP, San Antonio, TX, Amer. Meteor. Soc., J23-J24.

Bryan, K., 1969: A numerical method for the study of the circulation of the World Ocean. *J. Comp. Phys*, **4**, 347-376.

Chen, F., Z. Janjic and K. Mitchell, 1997: Impact of atmospheric surface–layer parameterization in the new land–surface

scheme of the NCEP mesoscale Eta model. *Boundary–Layer Meteorology* **48**, 391–421.

Gage, K.S., 1979: Evidence for a $k^{-5/3}$ Law Inertial Range in Mesoscale Two-Dimensional Turbulence. *J. Atmos. Sci.* **36**, 1950–1954.

Gage, K.S., Nastrom, G.D.. 1986: Theoretical Interpretation of Atmospheric Wavenumber Spectra of Wind and Temperature Observed by Commercial Aircraft During GASP. *J. Atmos. Sci*, **43**, 729–740.

Gallus W. A., Jr., 2000: The Impact of Step Orography on Flow in the Eta Model: Two Contrasting Examples. *Wea. and Forecasting*, 15, 630–639.

Gallus W. A., Jr. and J. B. Klemp, 2000: Behavior of Flow over Step Orography. *Mon. Wea. Rev.,* **128**, 1153–1164.

Gallus, W.A. and M. Rancic, 1996: A non-hydrostatic version of the NMC's regional Eta model. *Q. J.R. Meteorol. Soc.*, **122**, 495-513.

Gavrilov, M. B., 2002: Comments on "A More Extensive Investigation of the Use of Ensemble Forecasts for Dispersion Model Evaluation". *J. Appl. Meteorol.,* **41**, 899.

Gavrilov, M. B., 2004: A Note on Non-staggered Rectangular Grids Using Stream Function and Velocity Potential or Vorticity and Divergence. *Mon. Wea. Rev.*, **132**, in print.

Gavrilov, M. B. and Z. I. Janjic, 1989: Computed rotational energy spectra of two energy and enstrophy conserving schemes on semi-staggered grids. *Meteorol. Atmos. Phys.,* **41**, 1-4.

Janjic, Z. I., 1977: Pressure gradient force and advection scheme used for forecasting with steep and small scale topography. *Contrib. Atmos. Phys.*, **50**, 186–199.

_____, 1979: Forward–backward scheme modified to prevent two–grid–interval noise and its application in sigma coordinate models. *Contrib. Atmos. Phys.*, **52**, 69–84.

_____, 1984: Non–linear advection schemes and energy cascade on semi–staggered grids. *Mon. Wea. Rev.*, **112**, 1234–1245.

_____, 1990: The step–mountain coordinate: physical package. *Mon. Wea. Rev.*, **118**, 1429–1443.

_____, 1994: The step–mountain eta coordinate model: further developments of the convection, viscous sublayer and turbulence closure schemes. *Mon. Wea. Rev.*, **122**, 927–945.

_____, 1996a: The Mellor–Yamada level 2.5 scheme in the NCEP Eta model. 11th Conf. on NWP, Norfolk, VA, Amer. Meteor. Soc., 333–334.

_____, 1996b: The surface layer in the NCEP Eta model. 11th Conf. on NWP, Norfolk, VA, Amer. Meteor. Soc., 354–355.

_____, 1997: Advection scheme for passive substances in the NCEP Eta model. Research Activities in Atmospheric and Oceanic Modelling, WMO, Geneva, CAS/JSC WGNE, 3.14.

_____, 2000: Comments on "Development and Evaluation of a Convection Scheme for Use in Climate Models. *J. Atmos. Sci.*, **57**, p. 3686

_____, 2002: Nonsingular Implementation of the Mellor-Yamada Level 2.5 Scheme in the NCEP Meso model. NCEP Office Note No. 437, 61 pp.

_____, 2003: A Nonhydrostatic Model Based on a New Approach. *Meteorol. Atmos. Phys.*, **82**, 271-285.

Janjic, Z. and A. Wiin–Nielsen, 1977: On geostrophic adjustment and numerical procedures in a rotating fluid. *J. Atmos. Sci.*, **34**, 297–310.

Janjic, Z. I. and F. Mesinger, 1984: Finite-difference methods for the shallow water equations on various horizontal grids. *Numerical Methods for Weather Prediction,* Vol. 1, Seminar, ECMWF, 1983, Reading,

U.K., 29-101, Shinfield Park, Reading, Berkshire RG2 9AX, U.K.

Janjic, Z. I. and F. Mesinger, 1989: Response to small-scale forcing on two staggered grids used in finite-difference models of the atmosphere. *Quarterly Journal of the Royal Meteorological Society,* Vol. **115**, 1167-1176.

Janjic, Z. I., F. Mesinger and T. L. Black, 1995: The pressure advection term and additive splitting in split-explicit models. *Quarterly Journal of the Royal Meteorological Society,* **121**, 524, 953-957.

Janjic, Z. I., J. P. Gerrity, Jr. and S. Nickovic, 2001: An Alternative Approach to Nonhydrostatic Modeling. *Mon. Wea. Rev.,* **129**, 1164-1178.

Janjic, Z. I., and G. DiMego, 2001: Effects of Mountain Representation and Nonhydrostatic Dynamics in a Case of Orographic Precipitation. Symposium on Precipitation Extremes: Prediction, Impacts and Responses. 81st Annual Meeting of the Amer. Meteor. Soc., January 14-19, 2001, Albuquerque, NM, AMS, Boston, MA, 24-28.

Janjic, Z., T. Black, E. Rogers, H. Chuang, and G. DiMego, 2003: The NCEP Nonhydrostatic Mesoscale Forecasting Model. 10th Conference on Mesoscale Processes, Portland, OR, Amer. Meteor. Soc.

Lilly, D.K., 1983: Stratified Turbulence and the Mesoscale Variability of the Atmosphere. *J. Atmos. Sci,* **40**, 749–761.

Mesinger, F., Z.I. Janjic, S. Nickovic, D. Gavrilov and D.G. Deaven, 1988: The step–mountain coordinate: model description and performance for cases of Alpine lee cyclogenesis and for a case of an Appalachian redevelopment. *Mon. Wea. Rev.,* **116**, 1493–1518.

Nastrom, G.D., Gage, K.S., 1985: A Climatology of Atmospheric Wavenumber Spectra of Wind and Temperature Observed by Commercial Aircraft. *J. Atmos. Sci,* **42**, 950–960.

Phillips, N.A., 1957: A coordinate system having some special advantages for numerical forecasting. *J. Meteor.,* **14**, 184-185.

Simmons, A. J., and D. M. Burridge, 1981: An energy and angular-momentum conserving vertical finite-difference scheme and hybrid vertical coordinates. *Mon. Wea. Rev.,* **109**, 758-766.

Steppeler, Jürgen, Heinz-Werner Bitzer, Maud Minotte, Luca Bonaventura, 2002: Nonhydrostatic Atmospheric Modeling using a *z*-Coordinate Representation. *Mon. Wea. Rev.,* **130**, 2143–2149.

Straka, J.M., R.B. Wilhelmson, L.J. Wicker, J.R. Anderson and K.K. Droegemeier, 1993: Numerical solutions of a non-linear density current: a benchmark solution and comparisons. *Intl. J. Numerical Methods in Fluids,* **17**, 1-22.

Tung, Ka Kit, Orlando, Wendell Welch, 2003: The k^{-3} and $k^{-5/3}$ Energy Spectrum of Atmospheric Turbulence: Quasigeostrophic Two-Level Model Simulation. *J. Atmos. Sci,* **60**, 824–835.